Article

Blast wave characteristics under laser-driven in-tube accelerator operation conditions

Xilong Yu*,***, Toshiro Ohtani*, Sukyum Kim*,**, Toshihiro Ogawa*,
In-Seuck Jeung**, and Akihiro Sasoh*

*Institute of Fluid Science, Tohoku University, 2-1-1 Katahira, Sendai 980-8577, JAPAN
e-mail: sasoh@nana.ifs.tohoku.ac.jp

**Department of Aerospace Engineering, Seoul National University, Seoul 151-742, KOREA

***currently, Chinese Academy of Space Technology (CAST), Beijing,100080, CHINA

Received: May 21, 2004 Accepted: March 15, 2005

Abstract

Laser-driven blast waves and associated flow dynamics in the impulse generation processes of the laser-driven in-tube accelerator are studied through Schlieren visualization and streak spectroscopy. Three monatomic species, argon, krypton and xenon, are examined as the working gas. The laser pulse (wavelength; 10.6 μm, duration; 3 μs) is emitted from a carbon dioxide TEA (Transversely-Excited Atmospheric) laser. Being influenced by laser energy absorption processes, the shape of the laser-generated plasma has an aspherical shape. The speed of evolution of the blast wave is basically in proportion to the speed of sound, thereby being consistent to the experimentally-measured impulse characteristics. However, at where the plasma-laser coupling is strong, the larger the atomic number the higher a local shock Mach number becomes. Electronic-excitation energy distribution of argon ion at the focal point that is measured through emission spectroscopy exhibits nonequilibrium profile during a laser pulse irradiation period, then asymptotically approaches to equilibrium corresponding to an electronic excitation temperature of the order of 3 eV. After the blast wave gets reflected against a parabolic wall, its interaction with the plasma causes interface instability.

1. Introduction

Laser propulsion is a concept of propelling a vehicle using laser power. Its most important advantage is that a power supply does not need to be on board; the payload capability can be large. The cost for accessing a small vehicle to a space orbit can be made a couple of orders in magnitude lower than that with a conventional rocket system. The concept of laser propulsion was proposed in a technical paper first by Arthur Kantrowitz[1] in 1972. In 1990's, successful launches of a 'lightcraft' or its equivalent using repetitive-pulse (RP) lasers conducted by Myrabo et al.[2] and Schall et al.[3] demonstrated that this was really a feasible technology, thereby stimulating for further fundamental and practical researches. Moreover, increasing demands for "cheap" satellite launch and the developments of high power lasers and of related adaptive optics are further promoting the above-mentioned research activities.

The Laser-driven In-Tube Accelerator, which hereafter will be referred to as 'LITA'[4)-6)] is a unique device that accelerates a projectile in a tube. It combines the advantages of the ram accelerator[7] and laser propulsion concepts. Compared with conventional laser-launch in an open space, the impulse is significantly enhanced due to the high-pressure confinement effect in the closure space.[8] Moreover, the impulse is significantly increased when using the gas of a low speed of sound[5]. So far, the characteristics of LITA operation have been studied through measurements of an impulse and history of a pressure on the acceleration wall. This paper aims in better understanding detailed impulse generation mechanisms through flow visualization and emission spectroscopy, which will provide useful data for numerical simulation as well.

2. Experimental facility

The schematic of the experimental setup is shown in Fig. 1. The laser beam of a 30 mm × 30 mm square cross-section from a CO_2 TEA (transversely-excited atmospheric) laser (wavelength; 10.6 μm) is loosely focused with a ZnSe lens (focal length; f = 5 m, not shown in the figure), reflected on two molybdenum-coated mirrors (one of them is not shown in the figure), and then is introduced into a test chamber. The total laser energy that is effectively-

input to the test section, which is measured with an energy meter (Ed-500LIR, Gentec), equals 2.4 ± 0.2 J. The power history of a laser pulse is measured by introducing a peripheral of the laser beam to a photon drag sensor (B749, Hamamatsu Photonics K. K.). Figure 2 shows the history of the laser power and the energy fraction, which is the time-integration of the laser power normalized by the total laser energy. Hereafter, a time, t, is originated at the initiation of the laser beam irradiation. A 90 % of the total energy is concentrated in $t < 1.6$ μs. The first and highest power peak has a peak value of 13 MW; 45 % of the total energy is output during the first 0.2 μs. The power level after the first peak becomes one order in magnitude lower.

The test chamber has an inner rectangular volume of 256 mm × 80 mm × 80 mm. Five windows are fabricated. The laser beam passes through a 4-mm-thick NaCl window on the upper side of the test chamber. In order to project a laser beam only onto a parabolic mirror, a 16-mm-dia. iris is placed above the NaCl window. Framing Schlieren flow visualization is conducted using a pair of windows made of quartz, which plug over the ends of 80 mm × 80 mm cross-section. Radiation emission from a laser-generated plasma is collected through another quartz window.

In the test chamber, the collimated laser beam is reflected on a 16.2-mm-dia., aluminum-made parabolic mirror (focal length; 8.0 mm), then is point-focused at the center of the test chamber. The mirror is identical to that used in LITA impulse performance experiments[5]. The test chamber is connected to a rotary vacuum pump and a gas cylinder. A chamber pressure is measured using a Pirani and Bourdon tube pressure gauges. In the present experiments, either argon, krypton or xenon is used as the test gas. The fill pressure is set from 20 kPa to100 kPa.

As is shown in Fig. 1a, we visualize the generation and propagation of a blast wave with a Schlieren setup. A concave mirror of 1.0 m focal length collimates the light emitted from a xenon flash lamp (duration; 200 μs, SF200A, Nissin Electronic Co., energy; 200 J). Another concave mirror with a 2.54 m focal length, placed on the opposite side to the first mirror, collects the collimated light and images it onto a high-speed framing camera (Ultra 8, DRS Hadland Ltd., 10^8 frame s^{-1} at maximum, 8 frames). In order to avoid overexposure due to radiation emission from the laser-generated plasma, the distance from the test section to the second concave mirror is set to 3.8 m, which is much longer than its focal length. In order to further decrease the emission interference, a pinhole is set near the focal point of the concave mirror in front of the camera. This pinhole acts also as a circular knife edge; the visualization yields a Schlieren image.

An electronic-excitation temperature is simultaneously measured using a streak spectrograph (Hamamatsu Photonics K. K.). Radiation emission from the laser-generated plasma which is transmitted through the quartz window is collected using a quartz lens, optical fiber, and then to a monochromator. We use a 1200 g mm^{-1} grating with 10 μm slit width. The slit function is calibrated with a He-Ne 632.8 nm laser and fitted to a Gaussian function. The 1200 g mm^{-1} grating yields an approximately-linear dispersion in the exit plane of the monochromator, and the emission is captured through a streak tube and then onto an intensified charge-coupled device (ICCD) detector which

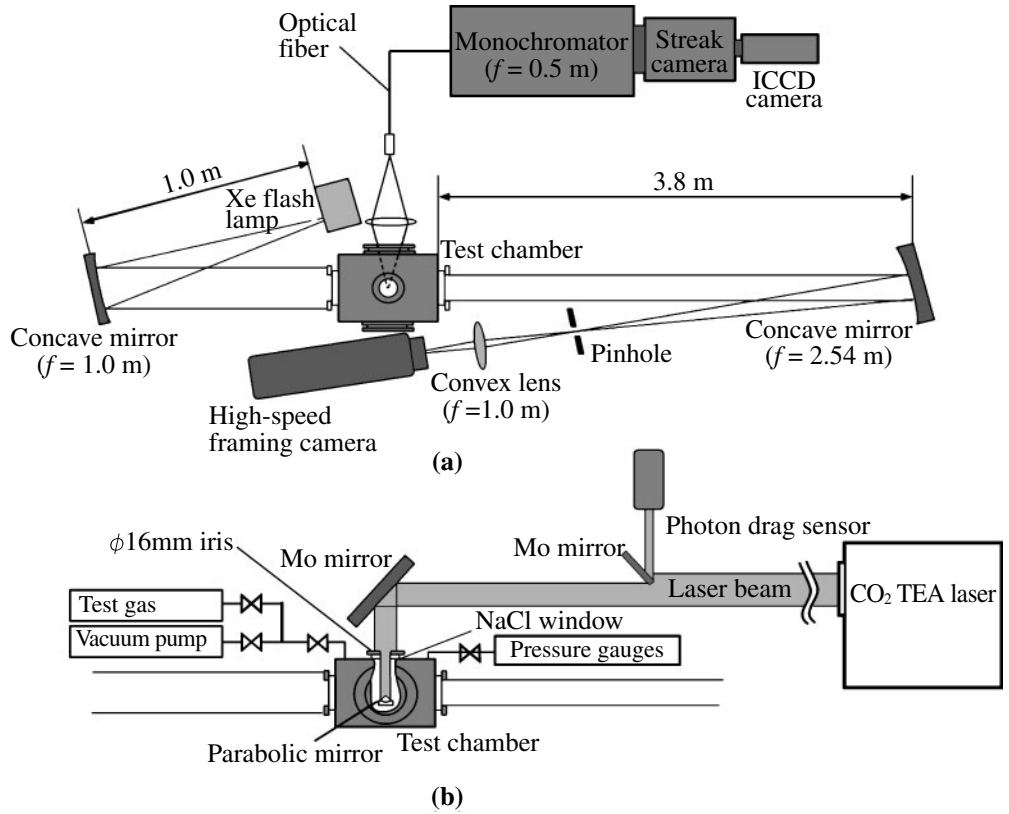

Fig.1 Experimental setup, (a) top view, (b) side view.

consists of 1280 × 1024 pixels. In an ICCD image, the abscissa of 1280 pixels represents a wavelength, the ordinate of 1024 pixels a time. The spectral resolution in the above-mentioned instrumental setup is 0.01 nm (pixel)$^{-1}$ and time resolution is about 7 pixel, corresponding to 70 ns in the time range of 10 μs. The spectral sensitivity of the whole system is calibrated by using a standard light source.

A series of trigger signals from a pulse generator (DG535, Stanford Research System, Inc.) with appropriate delay times are sent to the laser, the xenon flash lamp, the high-speed framing camera and the streak spectrograph system. All signals from the sensors are recorded in digital memory recorders (DL750 and DL1740, Yokogawa Electric Co.)

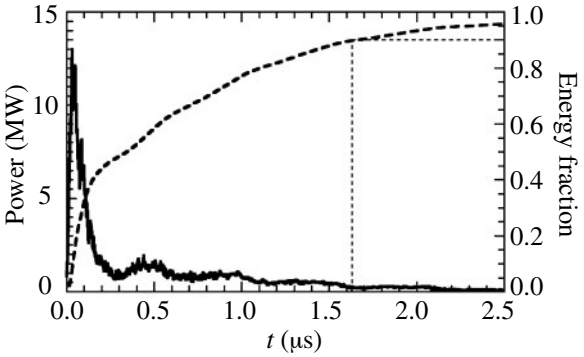

Fig. 2 Histories of laser power and corresponding energy fraction of the total energy, total energy; 2.4 J.

3. Results and discussion

3.1 Plasma core formation and expansion

Figure 3 shows an example of a set of sequential framing Schlieren images almost during a laser pulse duration. The location of the focus is shown in Fig. 3a (t = 0.06 μs); the orientation angle centered at the focus is also defined. Near the focus, the intensity of the laser beam becomes increased, causing breakdown in the test gas. Once it occurs the free

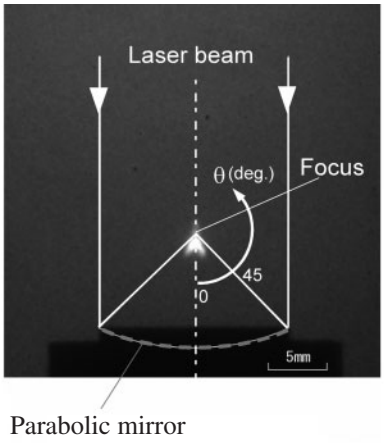

(a)

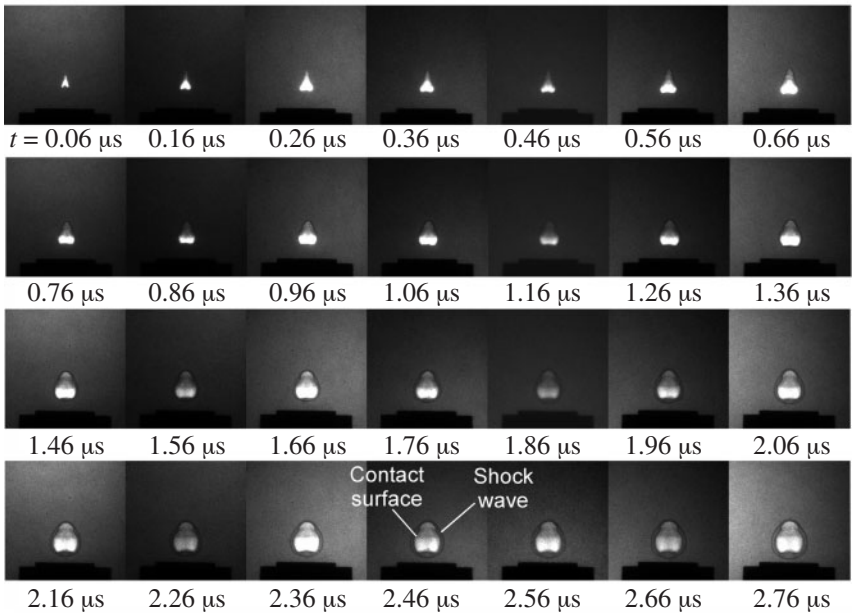

(b)

Fig. 3 Framing Schlieren images of laser generated plasma and blast wave during laser pulse duration, test gas; Ar, fill pressure;100 kPa, (a) laser beam ray superimposed on the frame at t = 0.06 μs, with definition of orientation angle, θ, (b) set of framing images, framing interval; 0.1μs, exposure time; 0.03 μs, the whole set of frames are taken from four independent laser pulse irradiations.

electron density increases through the so-called 'electron avalanche[9]', which in turn further enhances the absorption of the laser energy. As a result, a plasma core, which is recognized as a radiating region, is formed around the focus. The plasma core expands due to its localized high pressure, driving a shock wave outward.

It should be noted here that, the plasma core does not shape as a simple sphere but like a cone. After the breakdown, a part of the incident laser beam past the plasma core near the center axis is directly absorbed there. However, the peripheral part offset to the axis once passes by the focal region without significant absorption, reflected on the parabolic mirror, then being focused and absorbed in the plasma core. This portion of the blast wave proceeds over other because the blast wave gets enhanced due to the coupling with the absorbed laser power. Mori[10] et al. visualize a shock wave that is coupled with laser power absorption; the shock wave speed corresponds to a laser-supported detonation wave. In the present work, because the primary laser energy input terminates in about 0.3 μs, which corresponds to the first three frames in Fig. 3b. During that period, the plasma core and a blast wave are not separately visualized.

In the lower part of the plasma core, radiation emission is more intense and an expansion speed becomes higher. For $t < 1.0$ μs, a shock wave is observed to detach from the plasma core. Detailed processes of the blast wave propagation will be discussed in Sec. 3.3.

3.2 Electronic excitation temperature in plasma core

For a plasma in local thermodynamic equilibrium (LTE), the population distribution of electronic excitation energy levels follows Boltzmann profile expressed by[11]:

$$\ln\left(\frac{I_{ij}\lambda_{ij}}{g_i A_{ij}}\right) = C - \frac{E_i}{kT_e} \tag{1}$$

where i and j are indexes of upper and lower electronic states in transition, respectively, I; emission line intensity, λ; wavelength, g_i; statistical weight of upper level, A; transition probability for spontaneous emission (Einstein's A coefficient), E_i; energy of upper level, k; Boltzmann constant, T_e; electronic excitation temperature and C; constant.

Table 1 Spectroscopic data of Ar II for electronic excitation temperature measurements, National Institute of Standard Technology.

λ, nm	A_{ij},×10^{8}s^{-1}	E_i, eV	g_i
454.5052	0.471	19.86716	4
457.9349	0.801	19.97254	2
458.9898	0.664	21.12704	6
460.9567	0.789	21.14308	8
465.7901	0.892	19.80109	2
472.6868	0.588	19.76226	4
473.5905	0.58	19.26109	4
476.4864	0.64	19.86716	4
480.6020	0.78	19.22290	6

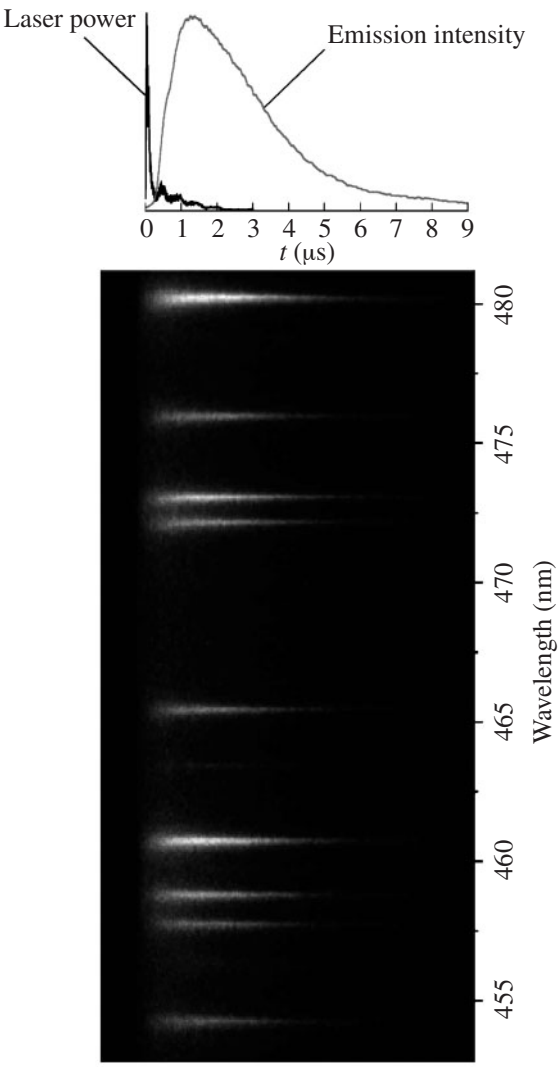

Fig. 4 Temporal streak image of emission spectra, Ar, P_0 = 20 kPa, with histories of emission intensity integrated with respect to wavelength from 453 nm to 481 nm and of laser power (timing error brought by jitter tolerance of streak spectrograph is ± 0.05 μs).

The wavelengths of spectroscopic lines and their upper level energy selected for excitation temperature determination are listed in Table 1. The wavelength range of the measurement is set to 28.3 nm centered at 467 nm, in which nine Ar II line spectra listed in Table 1 are covered.

Figure 4 shows an example of streak spectrograph of radiation emission from the focal point. Along a common time axis, t, the histories of the corresponding laser power and an emission intensity that is integrated with respect to wavelength are plotted. With respect to wavelength, the emission intensity of a 480.06 nm line is strongest. With respect to time, the integrated emission intensity has a maximum at a moment when the laser power almost vanishes. In other words, the emission intensity experiences time modulation from the laser pulse power; the time for peak shifts from t = 0.1 μs (laser power, see also Fig. 2) to t = 1.3 μs (emission), the effective duration from $\int I dt / I_{max}$ = 0.18 μs (laser) to 3.3 μs (emission).

Note here that the observation spot for the spectroscopy,

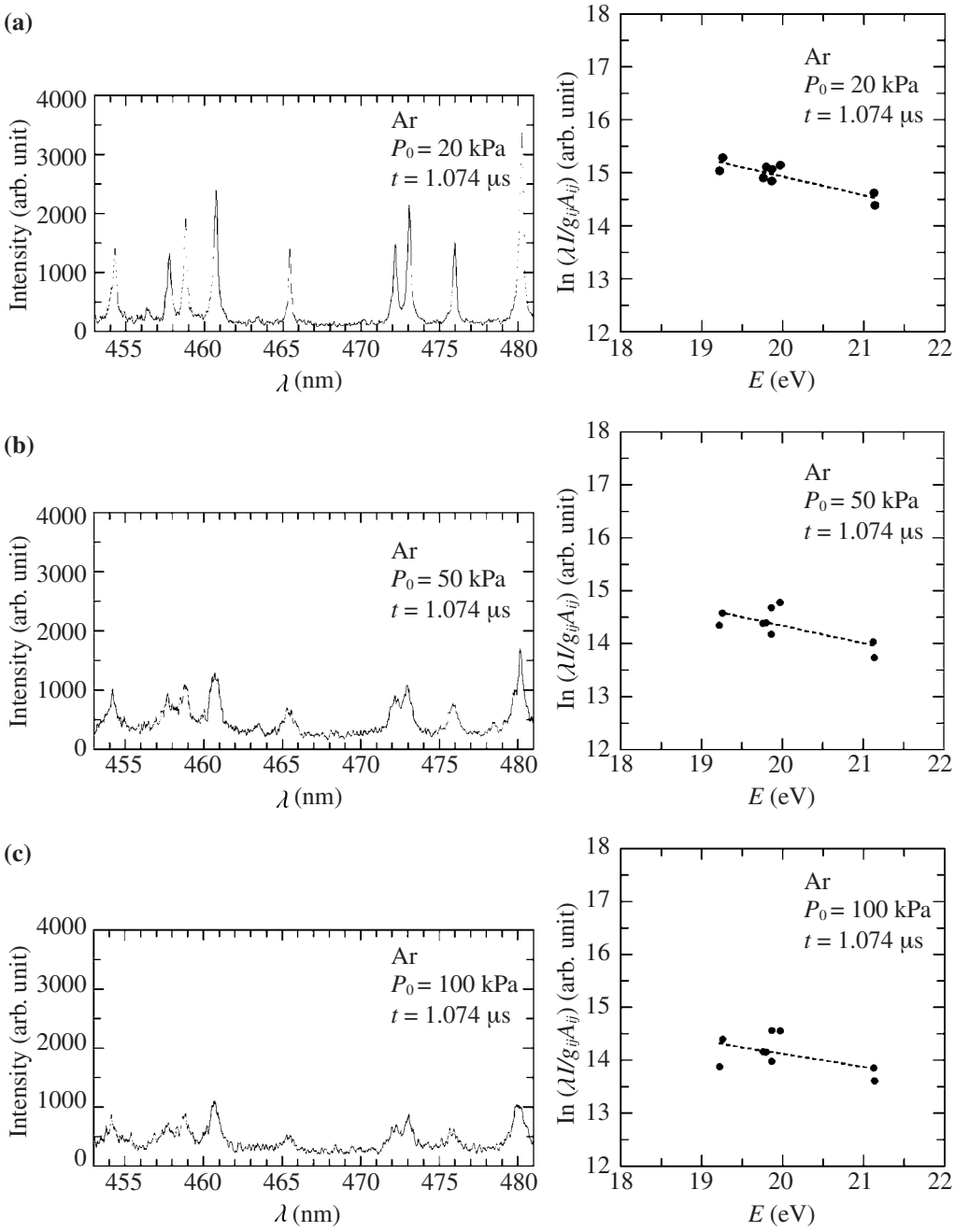

Fig. 5 Emission spectra (left, integration time, 0.01 μs) and corresponding Boltzmann plots (right), Ar, at t = 1.07 ± 0.05 μs, (a) P_0 = 20 kPa, (b) P_0 = 50 kPa, (c) P_0 = 100 kPa.

which has a spatial resolution of about 1 mm, is set to the focus of the parabolic mirror, and hence does not necessarily correspond to the location of a peak electronic excitation temperature. As is seen in Fig. 3b, during the laser pulse irradiation the shock wave is coupled with the laser beam, thereby yielding higher wave velocity towards the beam reflected from the parabolic mirror. The temperature distribution is expected to be considerably non-uniform.

In Fig. 5, emission spectra and corresponding Boltzmann plots for three different fill pressures, P_0, at the same t, are shown. Overall the emission intensity increases with decreasing P_0. When the same amount of laser energy is absorbed in an equal volume, the specific input energy in the volume is in inverse proportion to P_0; As shown in Fig. 5, for P_0 = 20 kPa the corresponding Boltzmann plot has a fitting line with smallest scatter, which corresponds to T_e = 3.5 ± 0.2 eV. On the other hand, for P_0 = 50 kPa and 100 kPa, because of a poor signal-to-noise ratio ascribed to a lower temperature, the scatter in the Boltzmann plot is so large that a temperature cannot be accurately obtained from the line fitting.

Figure 6 shows emission spectra and corresponding Boltzmann plots for P_0 = 20 kPa at different t. Figure 7 shows the history of T_e under the same condition as of Fig. 5a and 6. The uncertainly in determining an electronic excitation temperature is of the order of 0.4 eV at most. The temperature history exhibits a similar profile to that of the emission intensity shown in Fig. 4. The peak value of T_e is of the order of 3.5 eV.

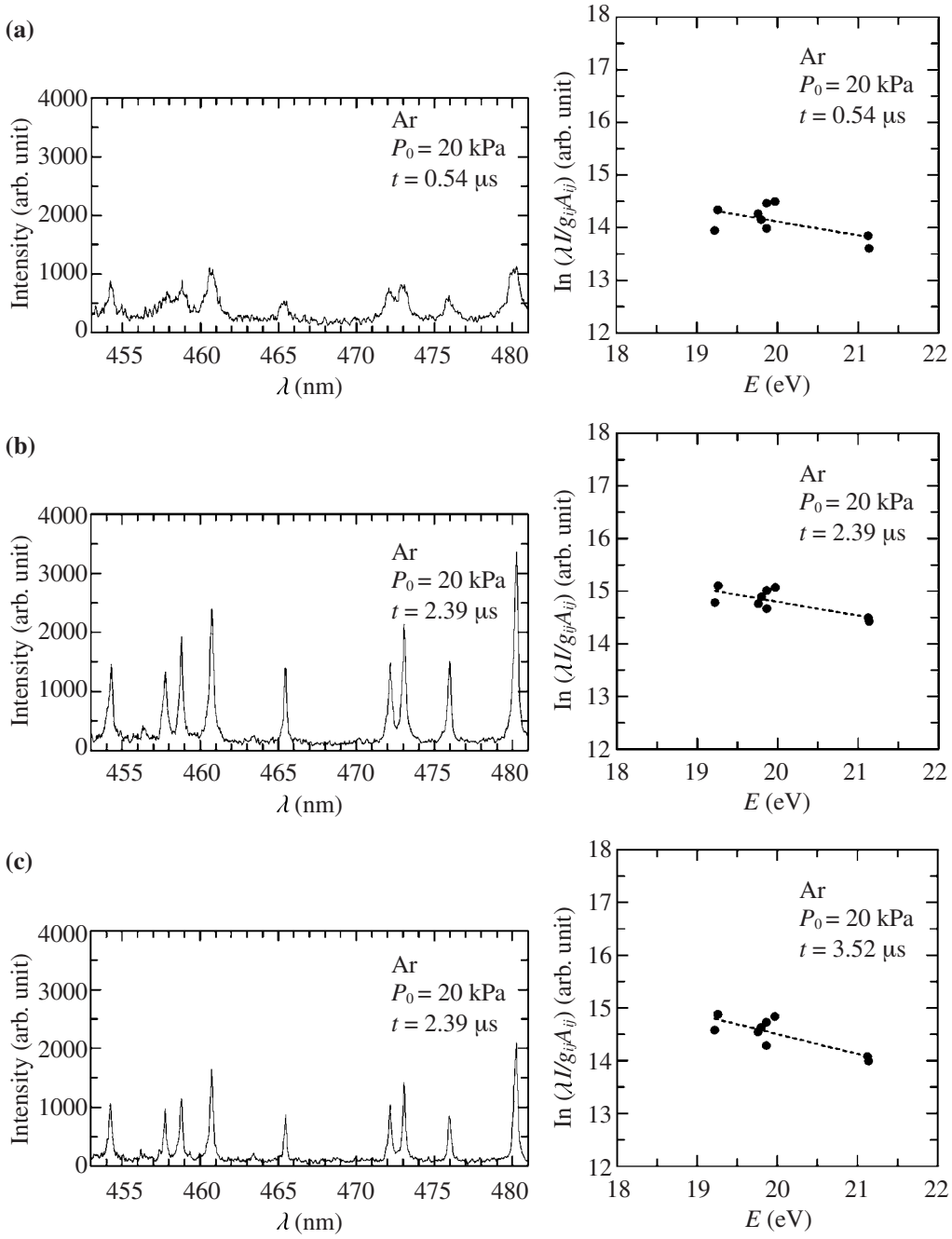

Fig. 6 Emission spectra (left, integration time, 0.01 μs) and corresponding Boltzmann plots (right) for Ar, P_0 = 20 kPa, (a) t = 0.54 ± 0.05 μs, (b) t = 2.39 ± 0.05 μs, (c) t = 3.52 ± 0.05 μs.

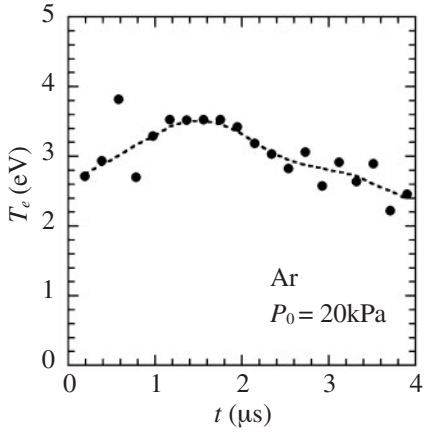

Fig. 7 Electronic excitation temperature history, Ar, P_0 = 20 kPa.

3.3 Spatiotemporal similarity linked to impulse characteristics

Figure 8 shows Schlieren images with different working gases at a delay time of t = 14.0 μs. The atomic masses of argon, krypton and xenon equal 39.95, 83.80 and 131.29g $(mol)^{-1}$, respectively. The smaller the atomic mass, the larger the size of the blast wave becomes. The speed of sound, a, at a constant room temperature is inversely proportional to the square root of the atomic mass. Therefore, the ratio of the speed of sound is 1.81 (Ar): 1.25 (Kr): 1.00 (Xe).

Sasoh et al[8]. discussed about the scaling relation with respect to time in the impulse generated by a laser-driven blast wave and following wave/flow motions. In their experiments using the laser-driven in-tube accelerator, the impulse is in proportion to the reciprocal of a. Moreover,

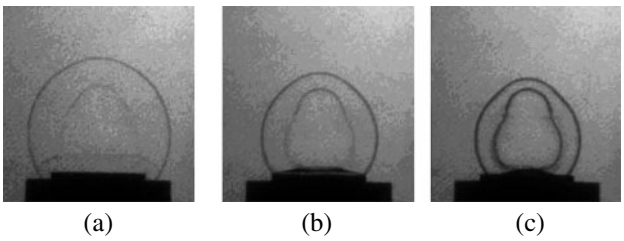

Fig. 8 Schlieren images at the same delay time after laser beam irradiation, $t = 14$ μs, exposure time; 0.03 μs, fill pressure; 100 kPa, (a) Ar, (b) Kr, and (c) Xe.

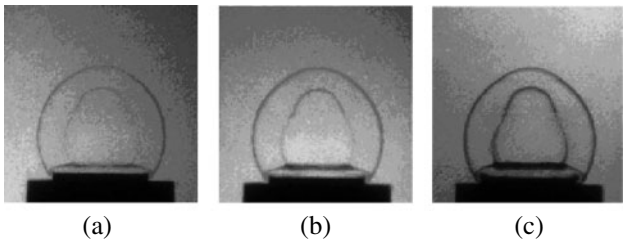

Fig. 9 Schlieren images at a constant value of $at = 3.83 \pm 0.06$ mm (a; speed of sound), exposure time; 0.03 μs, fill pressure; 100 kPa, (a) Ar, (b) Kr and (c) Xe.

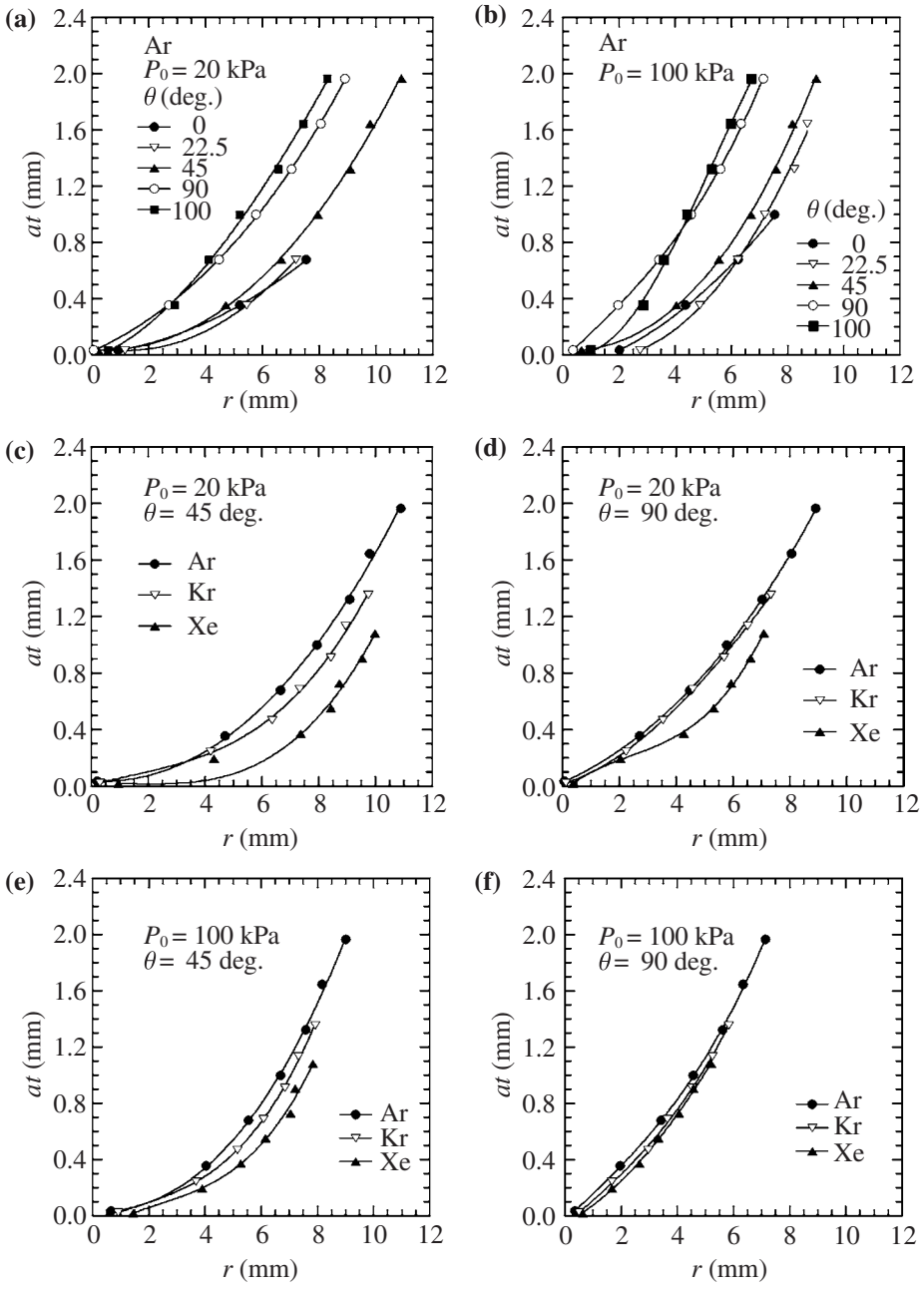

Fig. 10 Shock trajectories on at coordinate along several radial coordinates defined in Fig. 3a using their orientation angle, θ, (a) Ar, $P_0 = 20$ kPa, (b) Ar, $P_0 = 100$ kPa, (c) $P_0 = 20$ kPa, $\theta = 45$ deg. (d) $P_0 = 20$ kPa, $\theta = 90$ deg. (e) $P_0 = 100$ kPa, $\theta = 45$ deg. (f) $P_0 = 100$ kPa, $\theta = 90$ deg.

the pressure history measured on the acceleration tube wall becomes almost congruent on *at* coordinate[8]. Figure 9 shows Schlieren images for different gases but with a constant value of *at*: These wave patterns are almost congruent. It implies that the shock Mach number of the blast wave becomes almost independent of the species. From Rankine-Hugoniot relation for calorically perfect gas, the ratio of the post- to pre-shock pressures, P_2 and P_1 respectively, is a function only of a shock Mach number, M_S.

$$\frac{P_2}{P_1} = 1 + \frac{2\gamma}{\gamma+1}\left(M_S^2 - 1\right) \tag{2}$$

Since a local shock Mach number is independent of species, the post-shock pressure at a same distance from the focal point is independent of the species. Yet, it should be noted that the force exertion period is inversely proportional to *a*. The impulse onto the parabolic mirror is obtained as the spatial and temporal integration of the pressure over the mirror. On one hand, the spatial integration for a same value of *at* is independent of the species. On the other hand, the temporal integral is inversely proportional to *a*, then the impulse is also inversely proportional to *a*. Therefore, the self-similarity with respect to a speed of sound which was obtained in the measurements of the impulse and pressure on the acceleration tube wall[8] has been confirmed in the present independent experiments of the flow visualization.

In Fig.10, the trajectories of shock waves along several radial directions from the focus are plotted. Note here that the ordinate corresponds to *at*, which has a dimension of length; the slope in the plot corresponds to the reciprocal of a shock Mach number. As seen in Figs. 10a and 10b, for each initial pressure the shock wave propagates faster in the lower part, $\theta \leqq 45$ deg. Along $\theta = 22.5$ deg., the shock wave is most-strongly coupled with the laser power absorption, thereby obtaining fastest propagation speed in the beginning period. Along $\theta = 0$ deg., the shock speed becomes enhanced when the surrounding portion becomes focused and a Mach disk appears ($t = 1.36$ μs in Fig. 3b).

In Figs. 10c to 10f, the shock wave trajectories for different species are plotted. Along a radius on which the effect of plasma-laser coupling is small, $\theta = 90$ deg. (Figs. 10d and 10f), the trajectories are almost congruent except for Xe in Fig. 10d. However, along the strongly-coupled radial direction, $\theta = 45$ deg. (Figs. 10c and 10e), the larger the atomic mass, the faster the shock Mach number becomes. This implies that the effect of species appears where the laser-plasma coupling is significant although the above-mentioned similarity with respect to speed of sound basically holds. The possible reason for this tendency is that the larger the atomic mass, the smaller the ionization potential, thereby obtaining higher ionization rate and stronger energy coupling. The validation of this discussion warrants further analyses, in particular numerical ones.

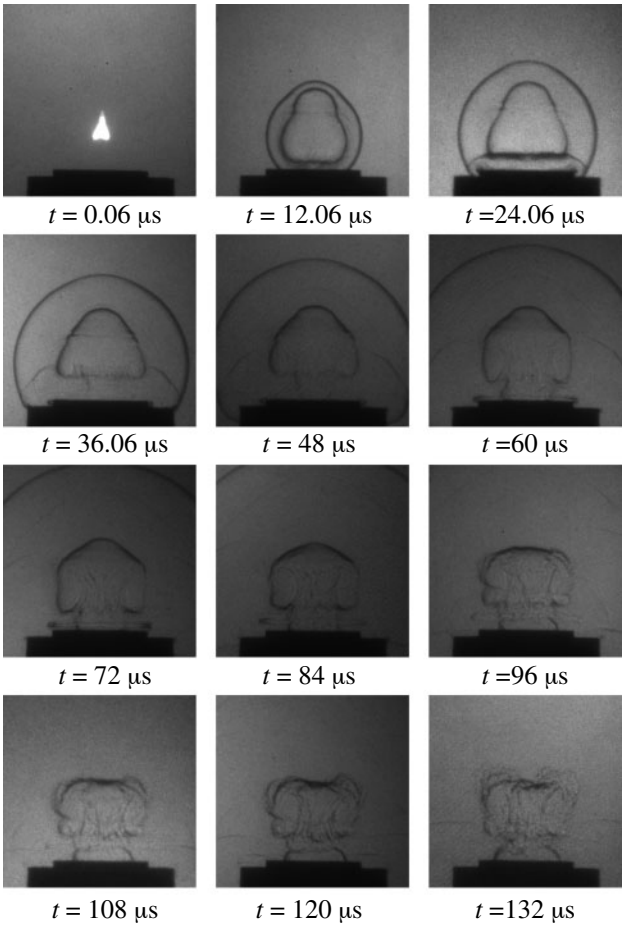

Fig. 11 Framing Schlieren images in a long period, Xe, $P_0 = 100$ kPa, framing interval; 12 μs, exposure time; 0.03 μs.

3.4 Instability due to plasma-shock interaction

Figure 11 shows the framing Schlieren images in a long period during which the interaction between the laser-generated plasma and a shock wave reflected against the parabolic mirror is observed. After the interaction, the contact surface gets deformed due to fluid dynamic instability, having a mushroom shape. The primary mechanism of the deformation is expected to be Richtmyer-Meshkov instability[12),13)]. The effect of the instability on the impulse characteristics is an important problem, however is beyond the scope of the present study.

4. Conclusion

Processes of laser plasma generation and following blast wave propagation under the laser-driven in-tube accelerator operation conditions are studied through flow visualization and spectroscopy. The shape of the plasma core which directly absorbs the laser pulse energy is affected by laser-plasma coupling, thereby considerably deviating from spherical symmetry. Yet, the blast wave incident onto the parabolic mirror basically follows the temporal scaling that the local shock Mach number is independent of a among the tested monatomic gases. This result is consistent to the impulse characteristic in the laser-driven in-tube accelerator. However, where the plasma-laser coupling is strong this similarity is slightly violated; the lower the ionization potential the higher the shock Mach number. Electronic excitation temperature is measured from emission spectra of Ar II lines. For a fill pressure of 20 kPa, a maximum temperature at the laser focal point becomes of the order of 3.5 eV. The flow visualization captures contact surface instability in the interaction between the laser-generated plasma and the reflected shock wave. The present study has provided experimental data useful for numerical simulation, which will yield further physical understandings of the impulse generation mechanisms in LITA.

Acknowledgements

The authors appreciate valuable discussion with Dr. Koichi Mori of Institute of Fluid Science, and valuable technical assistance from Mrs. T. Ogawa, K. Takahashi, M. Kato, K. Asano and N. Ito, Technical division of the institute.

References

1) A. Kantrowitz, Astronautics and Aeronautics, 10,74 (1972).
2) L. N. Myrabo, AIAA paper, AIAA-2001-3798.
3) W. O. Schall, W. L. Bohn, H.-A. Eckel, W. Mayerhofer, W. Riede, E. Zeyfang, High -Power Laser Ablation III., Proc. SPIE, 4065, pp. 472-481(2000).
4) A. Sasoh, Review of Scientific Instruments, 72,1893 (2000).
5) A. Sasoh, N. Urabe, S. S. Kim, I.-S. Jeung, Applied Phys A, 77,349 (2003).
6) A. Sasoh , J. Phys. IV France, 10,40 (2000).
7) A. Hertzberg, A. P. Bruckner, D. W. Bogdanoff, AIAA Journal,26,195 (1988).
8) A. Sasoh, N. Urabe, S. Kim, I.-S. Jeung, Transactions of the Japan Society for Aeronautical and Space Sciences, to be published.
9) Ya. B. Zel'dovich and Yu. P. Raizer, Physics of Shock Waves and High-Temperature Hydrodynamic Phenomena, Vol. I, Academic Press, New York, p. 360 (1996).
10) K. Mori, K. Komurasaki, Journal of Applied Physics, 92, 5563 (2002).
11) M. Hanafei et al., Radiation Physics and Chemistry, 57,11 (2000).
12) R. D. Richtmyer, Communications on Pure and Applied Mathematics, 13, 297-319 (1960).
13) E. E. Meshkov, Izv. Akad. Nauk, SSSR. M, 5, 151 (1969).